CHEMISTRY OF MATERIALS
Article

Chem. Mater. **2009,** *21,* 3763–3772 3763
DOI:10.1021/cm803510v

Nanostructured α-Fe_2O_3 Thin Films for Photoelectrochemical Hydrogen Generation

Asif Ali Tahir,[†] K. G. Upul Wijayantha,*[,†] Sina Saremi-Yarahmadi,[§] Muhammad Mazhar,[‡] and Vickie McKee[†]

[†]*Department of Chemistry, Loughborough University, Loughborough, Leics LE11 3TU, U.K.,* [‡]*Department of Chemistry, Quaid-I-Azam University, Islamabad 45320, Pakistan, and* [§]*Department of Materials, Loughborough University, Loughborough, Leics LE11 3TU, U.K.*

Received December 30, 2008. Revised Manuscript Received April 18, 2009

α-Fe_2O_3 thin film photoelectrodes were fabricated by aerosol-assisted chemical vapor deposition (AACVD) using a new hexanuclear iron precursor $[Fe_6(PhCOO)_{10}(acac)_2(O)_2(OH)_2]\cdot 3C_7H_8$ (**1**) (where PhCOO = benzoate and acac = 2,4-pentanedionate). The precursor (**1**) designed for AACVD has a low decomposition temperature and sufficient solubility in organic solvents and was synthesized by simple chemical techniques in high yield. It was characterized by melting point, FT-IR, X-ray crystallography, and thermogravimetry (TGA). The TGA analysis proved that complex (**1**) undergoes facile thermal decomposition at 475 °C to give iron oxide residue. In-house designed AACVD equipment was used to deposit highly crystalline thin films of α-Fe_2O_3 on fluorine-doped SnO_2 coated glass substrates at 475 °C in a single step. The material properties were characterized by XRD, XPS, and Raman spectroscopy, and the results confirmed that films were highly crystalline α-Fe_2O_3 and free from other phases of iron oxide. Further analysis of XRD data of the thin films proved the formation of crystalline hematite with an average diameter of 35 nm. X-ray photoelectron spectroscopy (XPS) confirmed that Fe is present only in the Fe^{3+} oxidation state. Scanning electron microscopy (SEM) showed that the needle-like particles having length in the range of 100 to 160 nm with a diameter of 30−50 nm are sintered together to form a compact structure of the 80-nm-thick α-Fe_2O_3 layer. Optical, electrical, and photoelectrochemical studies were conducted by UV−vis, electrochemical impedance spectroscopy, and steady-state current−voltage plots. The optical bandgap was estimated, and it is about 2.13 eV. The donor density of the α-Fe_2O_3 was 2.914×10^{23} m^{-3}, and the flatband potential is approximately −0.86 V vs $V_{Ag/AgCl}$. The photoelectrochemical characteristics recorded under AM 1.5 illumination indicated that the photocurrent density of 600 μA cm^{-2} at 1.23 V vs RHE, which is among the highest reported for an undoped α-Fe_2O_3 photoelectrode to date.

Introduction

Energy is the one of the greatest challenges before humanity in the 21st century. The primary purpose of most of the research activities in the field of energy technologies is to find a sustainable source which has the ability of meeting the growing demand in the decades ahead. Hydrogen, as a potential fuel for the future, has attracted significant interest in the past few years. More than 95% of the hydrogen consumed worldwide today is produced by a catalytic thermochemical conversion process which leads to a considerable amount of CO_2 emission.[1] Therefore, it disputes the prospect of hydrogen as an environmentally friendly energy source. Photochemical water splitting, however, is an environmentally sustainable route that uses the light energy from the sun to produce hydrogen by splitting water molecules.[2,3]

There has been considerable research activities in the discovery and design of suitable materials for photoelectrochemical (PEC) water splitting application since 1970s when preliminary work was first conducted by Fujishima and Honda.[4] The primary scientific and technological aim has been focused on finding materials that not only operate with high energy conversion efficiencies with operational stability but also can be prepared at relatively low cost. It is thus not surprising that α-Fe_2O_3 (hematite) has received considerable attention as a strong candidate material for water splitting photoelectrodes in recent years.[5−7] It is stable under illumination in aqueous solutions and has a bandgap energy of 2.1 eV which enables it to absorb considerable amounts of visible light (ca. 40% of incident solar radiation). The energy level of its valence band edge (1.6 V vs SCE at pH 14) also makes it suitable

*Corresponding author. E-mail: u.wijayantha@lboro.ac.uk.

(1) Ohi, J. *J. Mater. Res.* **2005**, *20*, 3180–3187.
(2) Osterloh, F. E. *Chem. Mater.* **2008**, *20*, 35–54.
(3) Woodhouse, M.; Herman, G. S.; Parkinson, B. A. *Chem. Mater.* **2005**, *17*, 4318–4324.
(4) Fujishima, A.; Honda, K. *Nature* **1972**, *238*, 37–38.
(5) Khan, S. U. M.; Akikusa, J. *J. Phys. Chem. B* **1999**, *103*, 7184–7189.
(6) Björkstén, U.; Moser, J.; Grätzel, M. *Chem. Mater.* **1994**, *6*, 858–863.
(7) Hu, Y.-S.; Kleiman-Shwarsctein, A.; Forman, A. J.; Hazen, D.; Park, J.-N.; McFarland, E. W. *Chem. Mater.* **2008**, *20*, 3803–3805.

Published on Web 07/29/2009

for initiating photoinduced oxygen evolution from water.[6,8] Moreover, it has recently been reported that nanostructured α-Fe_2O_3 thin films are suitable for developing multijunction hybrid photoelectrodes for hydrogen production.[9]

A variety of fabrication methods such as sol−gel,[10,11] reactive magnetron sputtering,[12] and aerosol/spray pyrolysis[13] have been used for the preparation of hematite thin films. It has been reported that the surface morphology and bulk composition of the films depends upon the deposition method and conditions, which significantly affect the PEC properties of α-Fe_2O_3 electrodes.[5,14,15] The unprecedented photocurrent performance reported by Kay et al.[16] recently has renewed interest in the fabrication of α-Fe_2O_3 photoelectrodes using chemical vapor deposition methods. In that work, authors reported Si doped α-Fe_2O_3 electrodes prepared by atmospheric pressure chemical vapor deposition (APCVD) with iron pentacarbonyl ($Fe(CO)_5$) as iron precursor and tetraethoxysilane (TEOS) as the Si precursor at 450 °C. In their APCVD process argon was bubbled through $Fe(CO)_5$ and TEOS at the rates of 11.3 mL/min and 19.4 mL/min, respectively. Both vapor streams were mixed with air at a flow rate of 2 L/min before the deposition took place on the heated substrate. The Si-doped electrodes produced in that method showed a photocurrent density of 2.3 mA/cm^2 at 1.23 V_{RHE}. The thermal decomposition of $Fe(CO)_5$ yields α-Fe_2O_3, along with the formation of iron metal and carbon monoxide.[16] A stringent requirement of the APCVD process is that the precursor material must have high enough vapor pressure. For example, the relatively high vapor pressure of $Fe(CO)_5$ (∼29 mmHg) positions it as an ideal precursor material for the deposition of α-Fe_2O_3 by APCVD. However, unlike $Fe(CO)_5$, almost all the other α-Fe_2O_3 CVD precursors (i.e., iron β-diketonates,[17] iron alkoxides,[18] and iron carboxylates)[19] possess negligible vapor pressures at room temperature, hence, unattractive for the APCVD process. The lack of suitable precursors has impeded further progress in preparation of nanostructured α-Fe_2O_3 photoelectrodes by APCVD. Therefore, the attention has been recently drawn to other CVD methods such as AACVD in which the vapor pressure of precursor materials is trivial.

Aerosol-assisted chemical vapor deposition (AACVD)[20] is a branch of CVD which is simple to operate and very versatile. In a typical AACVD process, the precursor solution remains at ambient temperature while the aerosol is generated using a piezoelectric transducer. The aerosol is then directed to the heated zone using a carrier gas. One of the advantages of AACVD is that a single solution source can be used to fabricate multicomponent layers ensuring both reproducibility and the presence of all the components in the deposited layer. Moreover, high quality thin films can be obtained by AACVD as the homogeneity of the aerosol can readily be controlled, and the size of the aerosol droplets is also closely controlled by the frequency of the ultrasonic generator. It also diminishes the volatility requirement of the precursor. The precursor is required to be merely soluble in a solvent from which an aerosol can be generated.[21,22]

In continuation of our recent work directed toward the fabrication of hematite electrodes for efficient photoelectrochemical hydrogen generation,[23−25] the current work is focused on synthesis of a single source precursor which is capable of delivering α-Fe_2O_3 to the target substrates such as fluorine doped SnO_2 coated glass (FTO) for deposition of thin film photoelectrodes. We synthesized a new iron carboxylate/β-diketonate precursor $[Fe_6(C_6H_5COO)_{10}(acac)_2(O)_2(OH)_2]\cdot 3C_7H_8$ (**1**) by mixing 2,4-pentanedione with $[Fe_3O(PhCOO)_6(Me_2O)_3]$-(PhCOO)] in toluene at room temperature to yield 96% of the product. We were thus able to enhance the solubility of the iron complex $[Fe_3O(PhCOO)_6(Me_2O)_3]$-(PhCOO)], which had a limited solubility in many organic solvents by the use of acetylacetonate ligand. The precursor (**1**) is readily soluble in common organic solvents such as toluene, THF, and alcohols, hence, an ideal candidate for the deposition of α-Fe_2O_3 thin films by AACVD. Although similar iron carboxylate complexes have been studied for molecular-based magnetic systems,[26,27] to our knowledge, such complexes have not been used for the deposition of α-Fe_2O_3 photoelectrodes for water splitting application.

Although adding various dopants (Si, Pt, Zn, Ti, etc.) to the α-Fe_2O_3 structure has been a popular strategy to enhance the photocurrent performance, the exact doping

(8) Sartoretti, J. C.; Ulmann, M.; Alexander, B. D.; Augustynski, J.; Weidenkaff, A. *Chem. Phys. Lett.* **2003**, *376*, 194–200.
(9) Miller, E. L.; Paluselli, D.; Marsen, B.; Rocheleau, R. E. *Sol. Energy Mater. Sol. Cells* **2005**, *88*, 131–144.
(10) Satsangi, V. R.; Kumari, S.; Singh, A. P.; Shrivastav, R.; Dass, S. *Int. J. Hydrogen Energy* **2008**, *33*, 312–318.
(11) Park, C.-D.; Magana, D.; Stiegman, A. E. *Chem. Mater.* **2007**, *19*, 677–683.
(12) Glasscock, J. A.; Barnes, P. R. F.; Plumb, I. C.; Savvides, N. *J. Phys. Chem. C* **2007**, *111*, 16477–16488.
(13) Desai, J. D.; Pathan, H. M.; Min, S.-K.; Jung, K.-D.; Joo, O.-S. *Semicond. Sci. Technol.* **2005**, *20*, 705–709.
(14) Sartoretti, C. J.; Alexander, B. D.; Solarska, R.; Rutkowska, I. A.; Augustynski, J. *J Phys. Chem. B* **2005**, *109*, 13685–13692.
(15) Ingler, W. B., Jr.; Baltrus, J. P.; Khan, S. U. M. *J. Am. Chem. Soc.* **2004**, *126*, 10238–10239.
(16) Kay, A.; Cesar, I.; Grätzel, M. *J. Am. Chem. Soc.* **2006**, *128*, 15714–15721.
(17) Martinez, A.; Pena, J.; Labeau, M.; Gonzalez-Calbet, J. M.; Vallet-Regi, M. *J. Mater. Res.* **1995**, *10*, 1307–1311.
(18) Mathur, S.; Veith, M.; Sivakov, V.; Shen, H.; Huch, V.; Hartmann, U.; Gao, H.-B. *Chem. Vap. Deposition* **2002**, *8*, 277–283.
(19) Basak, S.; Rane, K. S.; Biswas, P. *Chem. Mater.* **2008**, *20*, 4906–4914.
(20) Hou, X.; Choy, K.-L. *Chem. Vap. Deposition* **2006**, *12*, 583–596.
(21) Cross, W. B.; Parkin, I. P.; O'Neill, S. A.; Williams, P. A.; Mahon, M. F.; Molloy, K. C. *Chem. Mater.* **2003**, *15*, 2786–2796.
(22) Palgrave, R. G.; Parkin, I. P. *J. Mater. Chem.* **2004**, *14*, 2864–2867.
(23) Hiralal, P.; Unalan, H. E.; Wijayantha, K. G. U.; Kursumovic, A.; Jefferson, D.; MacManus-Driscoll, J. L.; Amaratunga, G. A. J. *Nanotechnology* **2008**, *19*, 455608.
(24) Saremi-Yarahmadi, S.; Tahir, A. A.; Vaidhyanathan, B.; Wijayantha, K. G. U. *Mater. Lett.* **2009**, *63*, 523–526.
(25) Saremi-Yarahmadi, S.; Wijayantha, K. G. U.; Tahir, A. A.; Vaidhyanathan, B. *J. Phys. Chem. C* **2009**, *113*, 4768–4778.
(26) McCusker, J. K.; Christmas, C. A.; Hagen, P. M.; Chadha, R. K.; Harvey, D. F; Hendrickson, D. N. *J. Am. Chem. Soc.* **1991**, *113*, 6114–6124.
(27) Canada-Vilalta, C.; O'Brien, T. A.; Brechin, E. K.; Pink, M.; Davidson, E. R.; Christou, G. *Inorg. Chem.* **2004**, *43*, 5505–5521.

Table 1. Summary of the Photocurrent Performance for Undoped α-Fe_2O_3 Electrodes Reported in Literature

authors/year	deposition method	photocurrent density ($\mu A/cm^2$)	potential	electrolyte	illumination source
this study	AACVD	600	1.23 V vs RHE	1 M NaOH	AM 1.5 (100 mW/cm^2)
Hu et al. 2008[7]	electrodeposition	690	0.4 V vs Ag/AgCl	1 M NaOH	410 mW/cm^2
Saremi-Yarahmadi et al. 2008[24]	APCVD	540	1.23 V vs RHE	1 M NaOH	AM 1.5 (100 mW/cm^2)
Kumari et al. 2007[28]	spray pyrolysis	60	0.7 V vs SCE	1 M NaOH	150 W WO_3 lamp
Kay et al. 2006[16]	APCVD	10	1.23 V vs RHE	1 M NaOH	AM 1.5 (100 mW/cm^2)
Sartoretti et al. 2005[14]	spray pyrolysis	780	0.45 V vs NHE	0.1 M NaOH	150 W Xe lamp
Glasscock et al. 2007[12]	spray pyrolysis	< 1	0.2 V vs SCE	1 M NaOH	AM 1.5 (100 mW/cm^2)
Sartoretti et al. 2003[8]	spray pyrolysis	100	0.2 V vs RHE	1 M NaOH	AM 1.5 (100 mW/cm^2)
Duret et al. 2005[29]	spray pyrolysis	14	1.2 V vs RHE	1 M NaOH	AM 1.5 (100 mW/cm^2)
//	ultrasonic spray pyrolysis	1070[a]			
Khan et al. 1999[5]	spray pyrolysis	2000	0.2 V vs SCE	1 M NaOH	50 mW, Xe lamp
Majumder et al. 1994[30]	spray pyrolysis	700	0.7 V vs NHE	NaOH+Na_2SO_4	200 W Xe lamp

[a] Although this performance was initially claimed for undoped α-Fe_2O_3, the authors later admitted that the sample was unintentionally doped with Si.[31]

mechanism, role of dopants, doping levels, and more importantly the stability of doped α-Fe_2O_3 photoelectrodes are still a subject of discussion.[14,12] It is known that the undoped α-Fe_2O_3 phototelectrode is free from such complications and photostable. Hence our present interest is to deposit undoped α-Fe_2O_3 photoelectrodes with improved PEC performance. The objective of this particular work is to report the PEC performance of undoped α-Fe_2O_3 deposited from precursor (**1**). The electrodes deposited from precursor (**1**) by AACVD show high photocurrent at 1.23 V vs RHE under AM 1.5 simulated light illumination. The results are compared to previous reported high photocurrent data for undoped α-Fe_2O_3. For the comparison, the photocurrent performance, deposition method, and measurement conditions reported for undoped α-Fe_2O_3 electrodes have been summarized in Table 1.

Experimental Section

Preparation and Characterization of Compounds. Solvents and reagents were obtained from commercial suppliers and used without further purification. The starting material $[Fe_3O(PhCOO)_6(Me_2O)_3](PhCOO)$ was prepared by following a literature method.[32] The FT-IR spectrum was recorded in the range 4000−250 cm^{-1} as KBr discs on a Mattson Cygnus 100 Fourier transform spectrometer. Controlled thermal analysis of the complex was investigated using a TA Instruments TGA 2950. The measurement was carried out in an alumina crucible under a nitrogen flow (60 mL/min) at a heating rate of 10 °C/min.

Synthesis and Characterization of the Precursor $[Fe_6(PhCOO)_{10}(acac)_2(O)_2(OH)_2]\cdot 3C_7H_8$ (1). A total of 1.67 g (4.18 mmol) of 2,4-pentanedione (acacH) was added to the suspension of 2.0 g (1.65 mmol) of $[Fe_3O(PhCOO)_6(Me_2CO)_3](PhCOO)$ in toluene at room temperature. After stirring for 2 h, the traces of $[Fe_3O(PhCOO)_6(Me_2CO)_3](PhCOO)$ were eliminated by filtration, and the reaction mixture was evaporated to dryness under reduced pressure. The solid was washed with hexane to remove the reaction byproduct and redissolved in 5 mL of toluene to give 95% of the crystalline product. Mp: 105 °C dec. Analysis. Calcd for $C_{80}H_{66}Fe_6O_{28}$: C, 53.01; H, 3.64. Found: C, 53.41; H, 3.80. FT-IR/cm^{-1} 3464br, 3064s, 2345w, 1967w, 1695w, 1599br, 1548s, 1493s, 1412br, 1361w, 1272s, 1176s, 1069s, 1025s, 934s, 839w, 817w, 786w, 716s, 687w, 673s, 647w, 594w, 561w, 548w, 484s, 435w, 352w, 325s, 301w, 264w.

Crystal data for $[Fe_6(C_6H_5COO)_{10}(acac)_2(O)_2(OH)_2]\cdot 3C_7H_8$: $C_{101}H_{90}Fe_6O_{28}$, fw 2086.83, space group $P\bar{1}$, a = 14.0386(13), b = 14.1668(13), c = 16.2804(15) Å, α = 90.891(2), β = 106.262(1), γ = 112.270(1)°, V = 2849.4(5) $Å^3$, Z = 1, ρ_{calcd} = 1.216 g cm^{-1}, μ = 0.810 mm^{-1}, 22797 reflections measured, 10033 unique (R_{int} = 0.0315), $wR2$ = 0.1190 (all data), $R1$ = 0.0438 ($I > 2\sigma(I)$). The data were collected at 150(2) K on a Bruker Apex II CCD diffractometer using Mo Kα radiation (λ = 0.71073 Å). The structure was solved by direct methods and refined on F^2 using the SHELXTL package.[33] All the nonhydrogen atoms were refined using anisotropic atomic displacement parameters, and hydrogen atoms were inserted at calculated positions using a riding model. The lattice contains severely disordered toluene solvate molecules which were treated using the PLATON SQUEEZE[34] procedure in WinGX.[35]

Deposition of Thin Films by AACVD. Commercially available FTO (TEC 8 Pilkington, 8 Ω/square) was used as the substracte. FTO substrates were ultrasonically cleaned with double distilled water, acetone, and propanol, and finally, they were washed with distilled water and stored in ethanol. The substrate slides (1 cm × 2 cm) were dried in air before use for the thin film deposition and placed inside the reactor chamber and then heated up to 475 °C for 20 min before the start of the deposition. In addition to the built-in thermometer, the temperature of the reactor chamber was also monitored by using an external thermocouple (type K) throughout the deposition. In a typical deposition, 0.1 g of the precursor was dissolved in 50 mL of toluene in a round-bottom flask. Air at a flow rate of 300 mL/min was used as the carrier, and the flow rate was controlled with the XL1 linear flowmeter. The aerosol was formed by keeping the flask in a water bath above the piezoelectric modulator of an ultrasonic humidifier (PIFCO ultrasonic humidifier). The precursor aerosol droplets generated were transferred into the hot wall zone of the reactor by the carrier gas, and the deposition

(28) Kumari, S.; Singh, A. P.; Tripathi, C.; Chauhan, D.; Dass, S.; Shrivastav, R.; Gupta, V.; Sreenivas, K.; Satsangi, V. R. *Int. J. Photoenergy* **2007**, Article ID No. 87467.
(29) Duret, A.; Grätzel, M. *J. Phys. Chem. B* **2005**, *109*, 17184–17191.
(30) Majumder, S. A.; Khan, S. U. M. *Int. J. Hydrogen Energy* **1994**, *19*, 881–887.
(31) Cesar, I.; Kay, A.; Martinez, J. A. G.; Grätzel, M. *J. Am. Chem. Soc.* **2006**, *128*, 4582–4583.
(32) Weinland, R. F.; Herz, A. *Eer. Dtsch. Chem. Ges.* **1912**, *45*, 2662–2668.
(33) Sheldrick, G. M. *SHELXTL*, Version 6.12; Bruker AXS: Madison WI, 2001
(34) Sluis, P. V. D.; Spek, A. L. *Acta Crystallogr.* **1990**, *A46*, 194–204.
(35) Farrugia, L. J. *J. Appl. Crystallogr.* **1999**, *32*, 837–838.

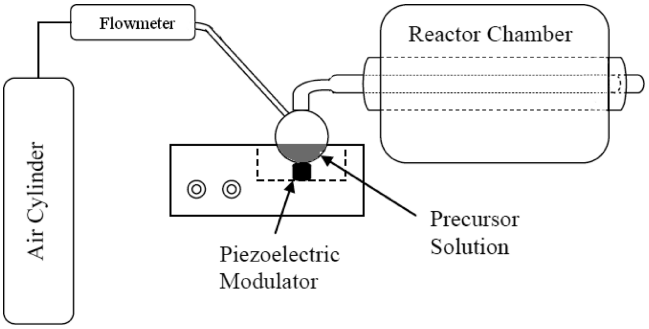

Figure 1. Schematic diagram of the AACVD setup.

was conducted for a period of 30 min. A schematic drawing of the AACVD apparatus is illustrated in Figure 1.

Structural Characterization. Phase and crystallinity of deposited films were characterized using Bruker AXS D8 Advance X-ray diffractometer with primary monochromatic high-intensity Cu Kα ($\lambda = 1.541$ Å) radiation with a PSD detector at the scan step of 0.007° and scan speed of 1 step/s. The surface morphology and film thickness were studied using a FEI Nova 600 Nanolab FIB/SEM system.

Surface Characterization. XPS spectra were recorded using a VG Scientific Escalab Mk I instrument operating with an unmonochromatised Al Kα X-ray source (1486.6 eV). Raman spectroscopy was undertaken using a HORIBA Jobin Yvon LabRAM HR (with 632.8 nm He−Ne laser) Raman spectrophotometer. The spectrum was recorded in the range of 100−1600 cm^{-1}.

Optical and Photoelectrochemical Characterization. Optical absorption measurements were performed using a Lambda 35 Perkin-Elmer UV−vis spectrophotometer to evaluate the optical properties of iron oxide thin films. An FTO glass substrate was placed in the reference optical path; thus, the absorbance measurements included only the contribution from iron oxide film.

Photocurrent was measured in a three-electrode configuration with 1 M NaOH as the electrolyte, Ag/AgCl/KCl as the reference electrode, and platinum wire as the counter electrode. The bare SnO_2 area of the hematite photoelectrode was used to make the electrical contact. The electrical contact with the α-Fe_2O_3 film was made with a gold-coated crocodile clip and kept above the level of electrolyte solution. The electrode potential was controlled by a potentiostat (micro-Autolab, type III) and is reported against the reversible hydrogen electrode (RHE). The Ag/AgCl was converted to RHE by using the following relation.[16]

$$E_{RHE} = E_{AgCl} + 0.059\text{pH} + E^{\circ}_{AgCl}$$

where

$$E^{\circ}_{AgCl} = 0.1976\ \text{V} \quad \text{at} \quad 25\ ^{\circ}\text{C}$$

In the electrochemical cell light enters through a quartz window and travels about a 5 mm path length in the electrolyte before illuminating the α-Fe_2O_3 photoelectrode. The electrode was illuminated through the electrolyte side, and the illumination area was 1 cm^2. The illumination source was an AM1.5 class A solar simulator (Solar Light 16S − 300 solar simulator). The voltage scan speed was 0.01 V/s, and light was manually chopped at regular intervals.

Electrical Measurements. Electrochemical impedance spectroscopic measurements were carried out in the dark to investigate electrical properties of the hematite films. The experiments were performed using a computer-controlled potentiostat (Autolab, PGSTAT12). The electrochemical cell was in the three electrode configuration as mentioned above. The superimposed ac signal was maintained at 20 mV while the frequency was scanned between 100 kHz and 100 Hz at potentials between −0.7 and 0 V vs $V_{Ag/AgCl}$ under dark. The data from the high frequency region, where the influence of the Helmholtz layer and surface states is minimal, were used to determine the space charge layer capacitance. The data obtained from the experiment were fitted to a simple equivalent circuit comprised of electrode and electrolyte resistances and space charge layer capacitance. The values for flatband potential (V_{fb}) and donor density (N_D) were calculated using the Mott−Schottky relationship (eq 1) and taking into account the intercept and the slope of the plot of $(1/C)^2$ vs applied voltage.

$$(1/C)^2 = 2(eN_D\varepsilon_0\varepsilon_r A^2)^{-1}(|V - V_{fb}| - kT/e) \qquad (1)$$

where A is the surface area of the film, ε_r is the dielectric constant of hematite (taken as 80)[36], ε_0 is the permittivity of free space, T is the temperature, and k is Boltzmann's constant.

Results and Discussion

Molecular Structure of $[Fe_6(PhCOO)_{10}(acac)_2(O)_2(OH)_2]\cdot 3C_7H_8$ (1). The structure of the centrosymmetric hexairon(III) complex is shown in Figure 2, and selected interatomic distances and angles are given in Table 2 (Supporting Information). It is a new member of a group of similar structures of general formula $[Fe_6(RCOO)_{10}O_2(OH)_2(X)_2]$ where X is a ligand providing one single-atom O bridge between two adjacent iron ions and one other donor; other examples include 2-(2-pyridyl)ethanoate,[27,37] 2-(*N*-methylimidazol-2-yl)-2-hydroxypropanoate,[38] 1,1-bis(*N*-methylimidazol-2-yl)ethanoate,[26] and 3-(2-hydroxypropylamino)-2-propanoate.[39] These complexes can be formally derived from the parent $[Fe_6(RCOO)_{12}O_2(OH)_2(L)_2]$ (where L = monodentate ligand) by substituting ligand X for two carboxylate/monodentate ligand combinations. Each benzoate ligand bridges two iron ions, as expected for the basic iron carboxylate derivatives. There has been considerable interest in the magnetostructural correlations in these complexes, and hence their structures have been extensively analyzed.[38,39] The iron-oxo core of the complex (Figure 3) is a typical example of the "planar" structural class.[38]

The core of the molecule is formed from two almost coplanar $\{Fe_3O\}^{7+}$ triangular units linked by the hydroxo groups O2 and O2′ which lie one on either side of the Fe_6 plane. The iron triangles are irregular with Fe−Fe distances ranging from 3.0442(6) to 3.5163(5) Å (Table 2 Supporting Information), and this is due to the presence

(36) Benko, F. A.; Longo, J.; Koffyberg, F. P. *J. Electrochem. Soc.* **1985**, *132*, 609–613.
(37) Canada-Vilalta, C.; Rumberger, E.; Brechin, E. K.; Wemsdorfer, W.; Folting, K.; Davidson, E. R.; Hendrickson, D. N.; Christou, G. *Dalton Trans.* **2002**, 4005–4010.
(38) Christmas, C. A.; Tsai, H.-L.; Pardi, L.; Kesselman, J. M.; Gantzel, P. K.; Chada, R. K.; Gatteschi, D.; Harvey, D. F.; Hendrickson, D. N. *J. Am. Chem. Soc.* **1993**, *115*, 12483–12490.
(39) Jones, L. F.; Jensen, P.; Moubaraki, B.; Cashlon, J. D.; Berry, K. J.; Murray, K. S. *Dalton Trans.* **2005**, 3344–3352.

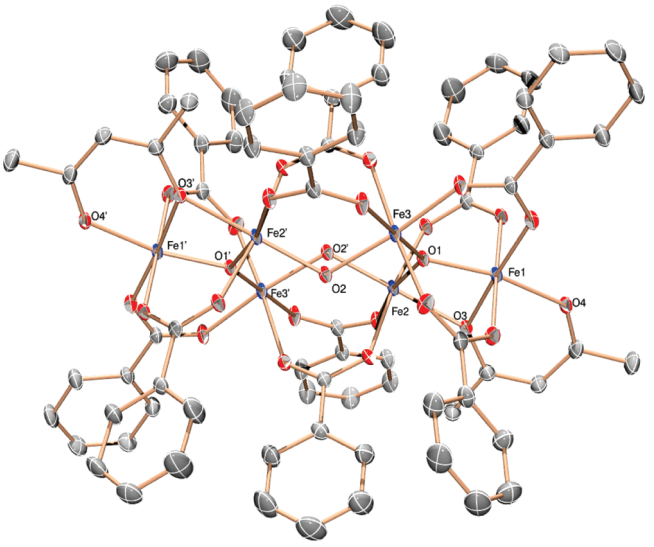

Figure 2. Molecular structure of $[Fe_6(PhCOO)_{10}(acac)_2(O)_2(OH)_2]$ (**1**). Ellipsoids are drawn at 30% probability level. The solvent (toluene) and hydrogen atoms are omitted for clarity.

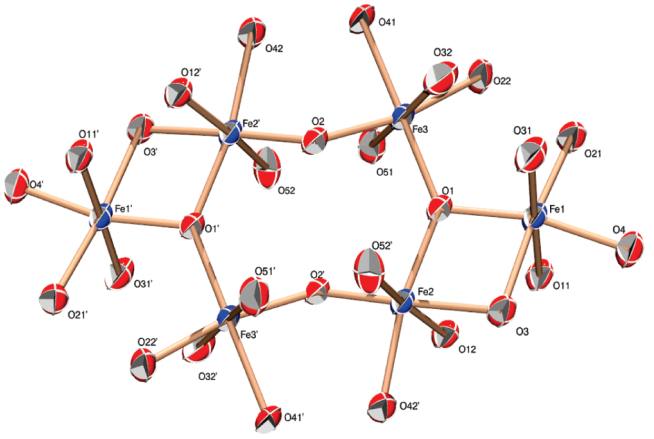

Figure 3. Fe/O core of $[Fe_6(PhCOO)_{10}(acac)_2(O)_2(OH)_2]$ (**1**). Ellipsoids are drawn at 50% probability level.

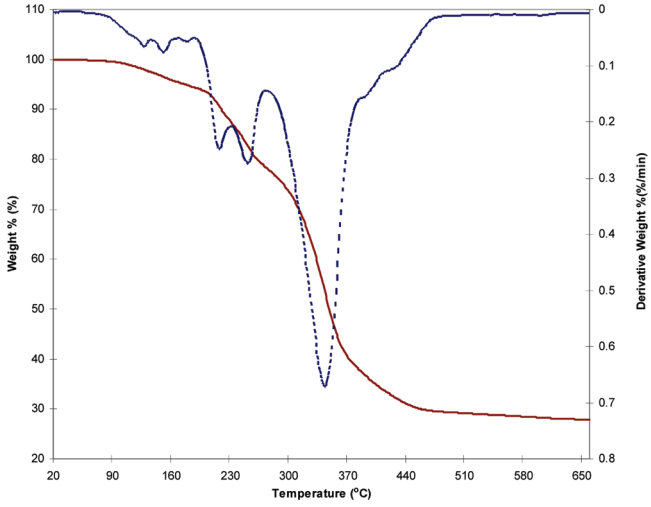

Figure 4. TGA/DTA plot, which shows the loss in weight with increase in temperature for precursor (**1**) at a heating rate of 10 °C/min under N_2.

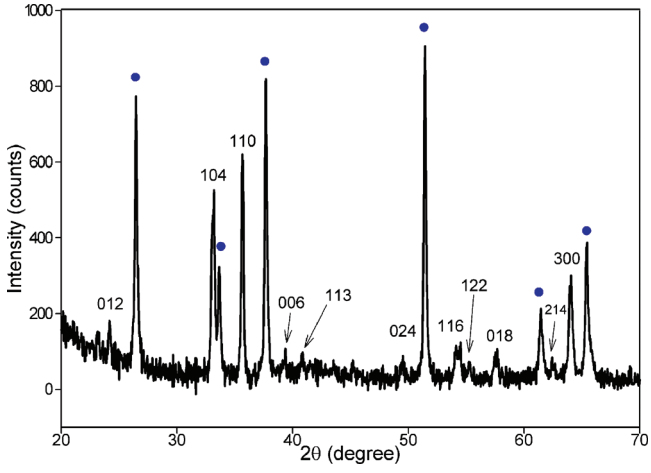

Figure 5. XRD patterns of α-Fe_2O_3 thin film deposited from precursor (**1**) at 475 °C on an FTO glass substrate: ● symbols indicate the peaks originated from SnO_2, and the others are related to the hematite phase.

of the single-atom bridge (O3) derived from the acac ligand. All the iron ions are six-coordinated, although there are some substantial deviations from octahedral geometry, particularly around Fe1 (e.g., O(1)−Fe(1)−O(21), 103.74(7)° and O(1)−Fe(1)−O(4), 165.20(7)°).

Thermal Decomposition Studies. The thermal decomposition of precursor (**1**) has been examined by thermogravimetric analysis, performed under a flow of N_2 (60 mL/min), at a heating rate of 10 °C/min. The TGA/DTA curve of precursor (**1**) shows five stages of weight loss (Figure 4). The first weight loss starts at 90 °C with a very small loss at 152 °C. The second step begins at 219 °C with a 14% of weight loss followed by the third step at 254 °C with a weight loss of 7%. The fourth step starts at 275 °C and completes at 385 °C, and maximum weight loss of 43% takes place during this step. This is directly followed by the final step which starts at 385 °C. The decomposition ends at about 475 °C. The resulting residue of about 26.42% of the initial mass is slightly less than the value of 26.54% calculated for complete conversion of precursor (**1**) to Fe_2O_3. Residual weight remains constant above 475 °C (recorded up to 650 °C) suggesting that the expected stable phase of Fe_2O_3 is achieved. The residual weight also indicates the complete decomposition of the organic groups. In complex **1**, each iron center is coordinatively saturated by the oxygen atoms of the chelating carboxylate and acac ligands, thus eliminating the need for additional oxygen to form oxides. The TGA proves that the new robust precursor is suitable for the deposition of α-Fe_2O_3 thin films at a relatively low temperature of 475 °C.

Structural Characterization. XRD was used to study the crystallinity of the deposited films. The XRD peak pattern is shown in Figure 5. The peaks indexed by the ● symbol correspond to the SnO_2 in the FTO substrate. The other four strong peaks, namely, (012), (104), (110) and (300), are the reflections of α-Fe_2O_3 (hematite). The presence of minor peaks such as (006), (113), (024), (116), (122), (018), and (214) provides further evidence for the existence of α-Fe_2O_3. The films deposited from precursor (**1**) are highly crystalline and free from other phases of iron oxide. The higher intensity of the (110)

peak indicates that the α-Fe_2O_3 particles are orientated in the 110 direction. The absence of peaks corresponding to other phases of iron oxide in the XRD data suggests that the precursor (**1**) is superior to a number of recently reported precursor materials for deposition of α-Fe_2O_3 thin films by CVD methods. For example, Shalini et al.[40] and Mathur et al.[41] used iron alkoxides for the deposition of α-Fe_2O_3, and their XRD analysis showed the formation of biphasic mixture of α-Fe_2O_3 and Fe_3O_4. Similarly, Ma et al.[42] and Martínez et al.[17] reported the deposition of α-Fe_2O_3 films using the Fe (β-diketonate) precursor and found that structural properties such as crystalline phase vary significantly against the deposition temperature, suggesting the temperature sensitivity of the decomposition of precursor. In a similar work Park et al.[43] reported the deposition of iron oxide from the Fe(II) dihydride CVD complex, and showed the requirement of a further post-annealing step to increase the crystallinity of the film. The precursor (**1**) reported in the present work not only permits the deposition of α-Fe_2O_3 thin films by a single AACVD step but also allows the desired films to be obtained without requiring any post annealing processes.

The volume average mean crystallite size, deduced from the broadening of the (110) diffraction peak by Scherrer equation,[44] is 35 nm, which is comparable to the average diameter of the particles estimated from SEM images.

An XPS spectrum was recorded to determine the oxidation states of Fe at the surface of the thin film of α-Fe_2O_3 deposited from precursor (**1**) and is shown in Figure 6. It has been reported that the peak position of Fe $2p_{3/2}$ is between 710.6 and 711.2 eV, the Fe $2p_{3/2}$ peak is narrower and stronger than Fe $2p_{1/2}$, and the area of Fe $2p_{3/2}$ peak is greater than that of Fe $2p_{1/2}$ because $2p_{3/2}$ has degeneracy of four states while $2p_{1/2}$ has only two in spin−orbit (j−j) coupling.[45−47] The Fe $2p_{3/2}$ peak has also been associated with a satellite peak located approximately 8 eV higher than the main Fe $2p_{3/2}$ peak for α-Fe_2O_3.[48] It has been previously reported that Fe $2p_{3/2}$ for Fe_3O_4 does not have a satellite peak.[49] The presence of the satellite peak in the present study (Figure 6) confirms the presence of α-Fe_2O_3. The binding energies of Fe $2p_{3/2}$ and Fe $2p_{1/2}$ obtained from the present study are 710.9 and 724.9 eV, respectively. The satellite peak obtained at 717.9 eV is clearly distinguishable and does not overlap either Fe $2p_{3/2}$ or Fe $2p_{1/2}$ peak.

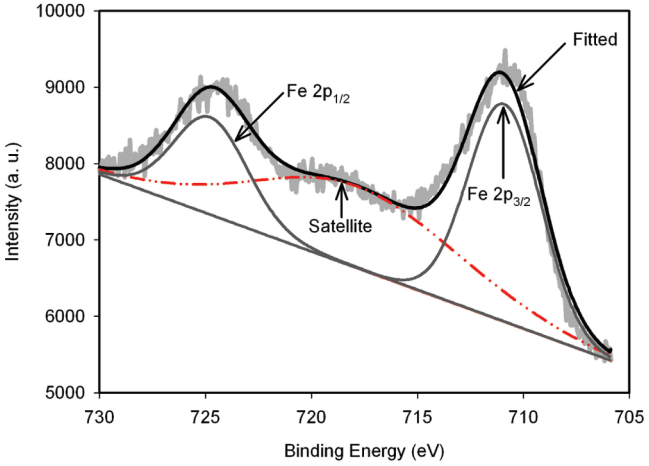

Figure 6. Fe 2p XPS spectrum of α-Fe_2O_3 thin film deposited from precursor (**1**) at 475 °C.

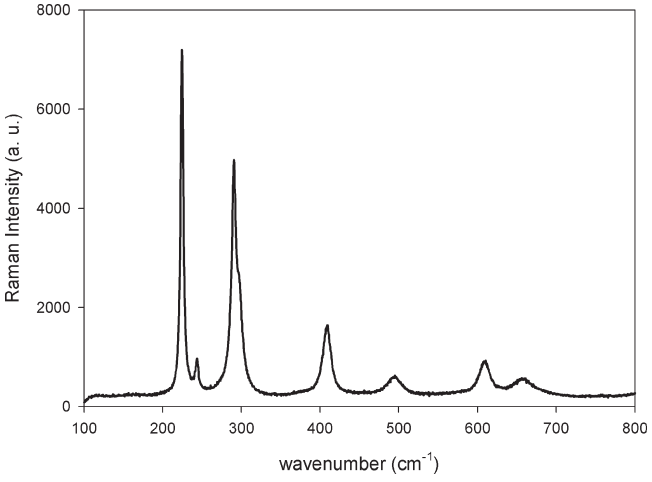

Figure 7. Raman spectrum of an α-Fe_2O_3 film deposited on a FTO glass substrate from precursor (**1**) at 475 °C.

Raman spectroscopy is often used to identify iron oxide phases, and the α-Fe_2O_3 spectrum is distinctly different from that of common impurity phases such as Fe_3O_4 and γ-Fe_2O_3.[50] The Raman spectrum of the α-Fe_2O_3 film deposited from precursor (**1**) on FTO glass substrate is shown in Figure 7. The spectrum is typical of α-Fe_2O_3 phase showing peaks at 224, 290, 409, 495, and 610 cm^{-1} and matched well with the previously reported Raman data for hematite.[51] The band around 660 cm^{-1} in the hematite spectrum has been reported by a number of studies and attributed to a large amount of defects, which would lead to a significant lattice distortion, as an evidence for the space-symmetry reduction and the appearance of this forbidden Raman mode.[51,52,25] Bersani et al.[53] also correlated crystallite size with the intensity of the band

(40) Shalini, K.; Subbanna, G. N.; Chandrasekaran, S.; Shivashankar, S. A. *Thin Solid Films* **2003**, *424*, 56–60.
(41) Mathur, S.; Sivakov, V.; Shen, H.; Barth, S.; Cavelius, C.; Nilsson, A.; Kuhn, P. *Thin Solid Films* **2006**, *502*, 88–93.
(42) Ma, T. Y.; Lee, I. C. *J. Mater. Sci.: Mater. Electr.* **2004**, *15*, 775–780.
(43) Park, S.; Lim, S.; Choi, H. *Chem. Mater.* **2006**, *18*, 5150–5152.
(44) Cabanas, M. V.; Vallet-Regi, M.; Labeau, M.; Gonzalez-Calbet, J. M. *J. Mater. Res.* **1993**, *8*, 2694–2701.
(45) Kuivila, C. S.; Butt, J. B.; Stair, P. C. *Appl. Surf. Sci.* **1988**, *32*, 99–121.
(46) Grosvenor, A. P.; Kobe, B. A.; Biesinger, M. C.; McIntyre, N. S. *Surf. Interface Anal.* **2004**, *36*, 1564–1574.
(47) Yamashita, T.; Hayes, P. *Appl. Surf. Sci.* **2008**, *254*, 2441–2449.
(48) Muhler, M.; Schlögl, R.; Ertl, G. *J. Catal.* **1992**, *138*, 413–444.
(49) Hawn, D. D.; DeKoven, B. M. *Surf. Interface Anal.* **1987**, *10*, 63–74.
(50) de Faria, D. L. A.; Silva, S. V.; de Oliveira, M. T. *J. Raman Spectrosc.* **1997**, *28*, 873–878.
(51) Glasscock, J. A.; Barnes, P. R. F.; Plumb, I. C.; Bendavid, A.; Martin, P. J. *Thin Solid Films* **2008**, *516*, 1716–1724.
(52) Pérez León, C.; Kado, L.; Zhang, M.; Müller, A. H. E. *J. Raman Spectrosc.* **2004**, *35*, 165–169.
(53) Bersani, D.; Lottici, P. P.; Montenero, A. *J. Raman Spectrosc.* **1999**, *30*, 355–360.

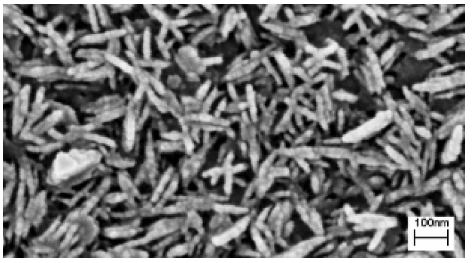

Figure 8. Top view of the surface of α-Fe_2O_3 thin film showing the needle-like structures at the surface of the film.

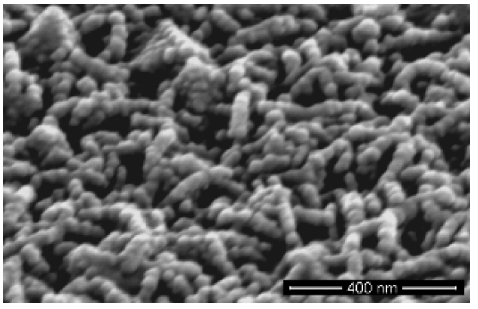

Figure 9. Surface morphology of the α-Fe_2O_3 thin film tilted at 52°. The image shows the formation of needle-like nanostructures as a result of the incorporation of small individual nanoparticles.

around 660 cm^{-1}, which suggests that this band may be related in particular to surface and grain boundary disorder.

Surface Morphology and Cross-Section Measurements of the Thin Film. The surface morphology of the film was determined by FIB/SEM, and the results are shown in Figures 8−10. As illustrated in Figure 8, the surface of the film consists of small needle-like nanostructures. The length of each needle is in the range of 100−160 nm with a diameter of 30−50 nm. Each needle-like nanostructure is a result of the incorporation and agglomeration of ~35 nm individual particles, and Figure 9 provides clear evidence for that. Individual needles are fused to each other forming an interconnected 3D network with electronic connections to facilitate the photoinduced charge transport. The cross-sectional image of the film (Figure 10) further reveals that the mesoscopic needles are sintered together to form a compact structure with the thickness of ~80 nm. Figure 10 confirms that the film thickness is uniform throughout the layer.

The presence of a number of strong diffraction patterns of hematite in the XRD data confirms that deposited thin films are highly crystalline (unless the films are highly crystalline, it is very unlikely to obtain such strong diffraction data for hematite deposited on FTO, when it considers the thickness of hematite and FTO layers which are about 80 and 600 nm, respectively). The nanostructured α-Fe_2O_3 electrodes of this nature contain unique physical and chemical properties that are essential for photoelectrochemical water splitting devices. The formation of needle-like nanostructures by interconnecting with adjacent individual particles provides a large surface area which is beneficial for light-induced charge transfer at the surface of α-Fe_2O_3. The dimensions of each crystallite of the

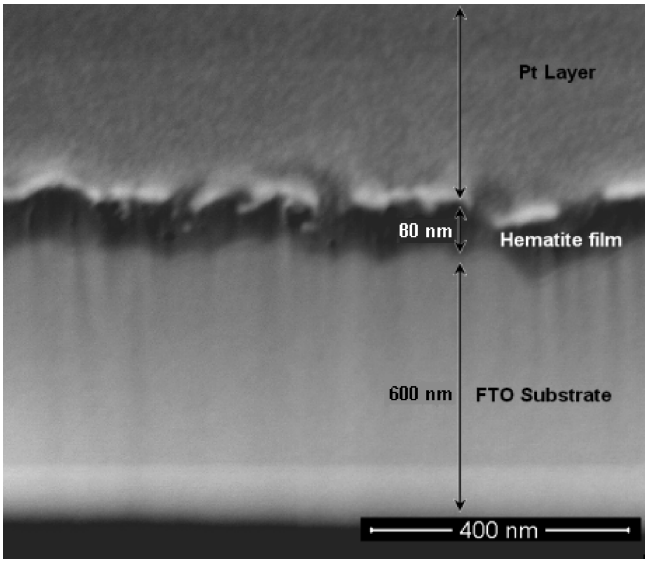

Figure 10. Cross-sectional SEM image of an α-Fe_2O_3 layer on FTO-coated glass.

photoelectrode (each needle length is 100−160 nm and diameter is 30−50 nm) are well above the hole diffusion length of hematite (ca. 2−4 nm).[6] Therefore, the recombination of photogenerated charges within each individual crystallite could be high. Considering the light absorption coefficient of hematite which is of the order of 2.3×10^5 cm^{-1}, at least a 430 nm thick layer is required to absorb most of the light.[51] Therefore, as expected, our attempts of increasing the film thickness that consists of individual crystallites of the order of 100−160 nm long and 30−50 nm diameter, from its current value (~80 nm) toward the optimum film thickness, did not yield higher photocurrent. Nevertheless, our work opens a new route to exploit novel precursor materials by AACVD to make α-Fe_2O_3 electrodes with better photoelectrochemical performance. In fact, our future work is directed to enhance the capabilities of the AACVD method so that using the precursor (**1**) the dimensions of crystallites can be tuned to obtain structures comparable to the hole diffusion length of hematite which will allow us to increase the film thickness to harness all visible light up to the optical absorption threshold of α-Fe_2O_3 (ca. 570 nm).

Optical Characterization. The nanostructured α-Fe_2O_3 film deposited by AACVD was translucent and reddish brown in color. The optical absorption spectrum is shown in Figure 11. The absorption gradually decreases as the wavelength extends toward the visible region. From 540−600 nm the absorption decreases significantly and becomes linear into the red region. The presence of an absorption tail between 540 and 600 nm probably indicates the existence of sub-bandgap states.[54]

The Tauc plot shows the relationship between the incident photon energy ($h\nu$) and the absorption coefficient (α) near the absorption edge. The optical bandgap (E_g) can be calculated according to following equation

(54) Beermann, N.; Vayssieres, L.; Lindquist, S.-E.; Hagfeldt, A. *J. Electrochem. Soc.* **2000**, *147*, 2456–2462.

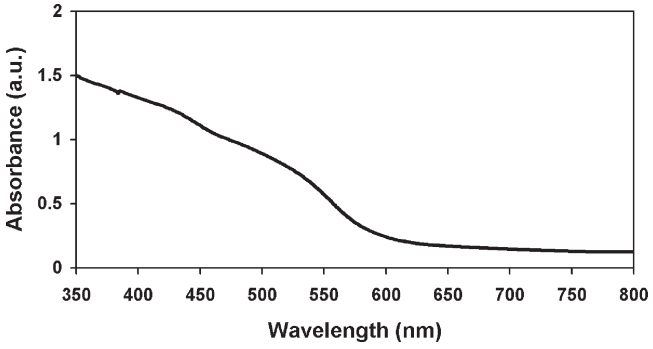

Figure 11. Optical absorption spectrum of α-Fe_2O_3 film deposited from precursor (**1**) by AACVD.

$$\alpha h\nu = A_0(h\nu - E_g)^n \quad (2)$$

where

$$A_0 = \left[\frac{e^2}{nch^2 m_e^*}\right](2m_r)^{3/2} \quad (3)$$

where m_e^* and m_r are the effective and reduced masses of charge carriers, respectively, and n depends on the nature of band transition, $n = 1/2$ or $3/2$ for direct allowed and forbidden transitions and $n = 2$ or 3 for indirect allowed and indirect forbidden transitions, respectively. The indirect bandgap is estimated from the intercept of the extrapolated linear fit to the experimental data of $(\alpha h\nu)^2$ vs photon energy plot. From the indirect transition, the bandgap of 2.13 eV is estimated by extrapolating the linear part of the graph as shown in Figure 12. This value agrees well with previously reported values of 1.9 to 2.2 eV depending on crystalline status and methods of preparation of α-Fe_2O_3 thin films.[55−57]

Photoelectrochemical Characterization. The photoelectrochemical measurements were performed in a 1 M NaOH aqueous solution by illuminating the α-Fe_2O_3 electrode from the electrolyte side with 1.5 AM simulated light. The photocurrent density (J) is plotted against applied bias potential (V) and shown in Figure 13. The steady state photocurrent onset estimated from the J^2-V plot was at 0.78 V vs RHE. A photocurrent density of 600 μA cm^{-2} was achieved at 1.23 V vs RHE while no dark current was observed up to about 1.6 V where oxygen evolution normally begins. The photocurrent density rises steeply up to approximately 1.2 mA cm^{-2} without reaching the saturation. As shown in Figure 13 the photocurrent density recorded under the steady-state conditions is slightly lower than that of its transient counterparts at applied potential below 1.1 V. This indicates that the recombination is relatively high in the region where the space charge layer width is relatively narrow. However, as the applied potential increases above 1.1 V, the photocurrent pulses acquire the desirable

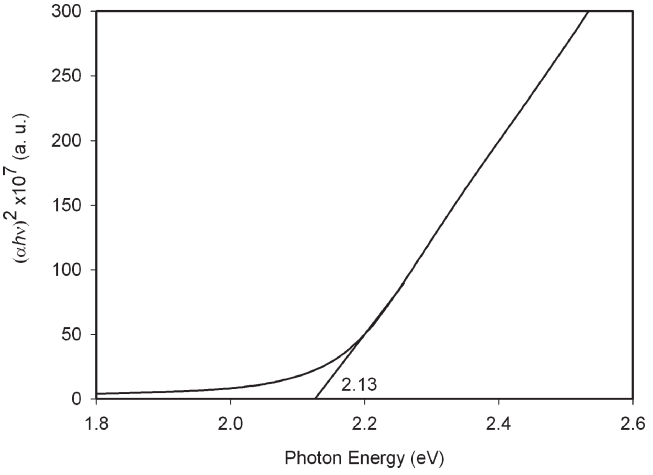

Figure 12. Tauc plot showing the calculated optical bandgap of 2.13 eV for α−Fe_2O_3 film deposited from precursor (**1**) by AACVD.

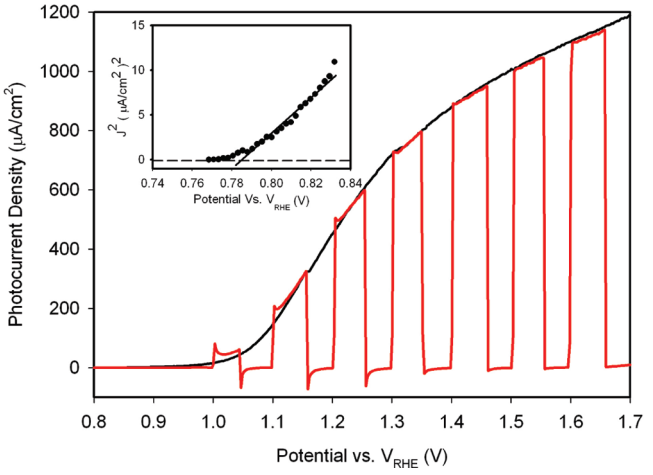

Figure 13. Steady-state and transient photocurrent potential curves for the α-Fe_2O_3 thin film deposited from precursor (**1**) at 475 °C measured in 1 M NaOH under simulated AM 1.5 sunlight. The scan rate is 0.01 V/s. The J^2-V plot in the inset shows photocurrent onset.

square shapes and agree with the steady-state photocurrent. The photocurrent value recorded for the photoelectrode deposited from precursor (**1**) is among the highest reported to date for the undoped α-Fe_2O_3 photoelectrodes prepared by any deposition method (see Table 1).

Electrical Characterization. The electrochemical impedance spectrum recorded at −0.5 V vs $V_{Ag/AgCl}$ is shown in Figure 14a. Impedance measurements were conducted in the range between −0.7 and 0 V vs $V_{Ag/AgCl}$ where the electrode is in the depletion region. The Mott−Schottky plot shown in Figure 14b was constructed by using the space charge capacitance values estimated by fitting the impedance responses to a series-parallel RC equivalent circuit using a nonlinear least-squares method. It is well-known that factors such as the surface roughness of the electrode,[58] deep traps or surface state interactions,[59] and specific conductivity of electrolyte solution[60]

(55) Akl, A. A. *Appl. Surf. Sci.* **2004**, *233*, 307–319.
(56) Ozer, N.; Tepehan, F.; Tepehan, G. *Proc. SPIE—Int. Soc. Opt. Eng. (USA)* **1997**, *3138*, 9–31.
(57) Vayssieres, L.; Sathe, C.; Butorin, S. M.; Shuh, D. K.; Nordgren, J.; Guo, J. *Adv. Mater. (Weinheim, Ger.)* **2005**, *17*, 2320–2323.
(58) Wang, Y.-B.; Yuan, R.-K.; Willander, M. *Appl. Phys. A: Mater. Sci. Process.* **1996**, *63*, 481–486.
(59) Schefold, J. *J. Electroanal. Chem.* **1993**, *362*, 97–108.
(60) Oskam, G.; Vanmaekelbergh, D.; Kelly, J. J. *J. Electroanal. Chem.* **1991**, *315*, 65–85.

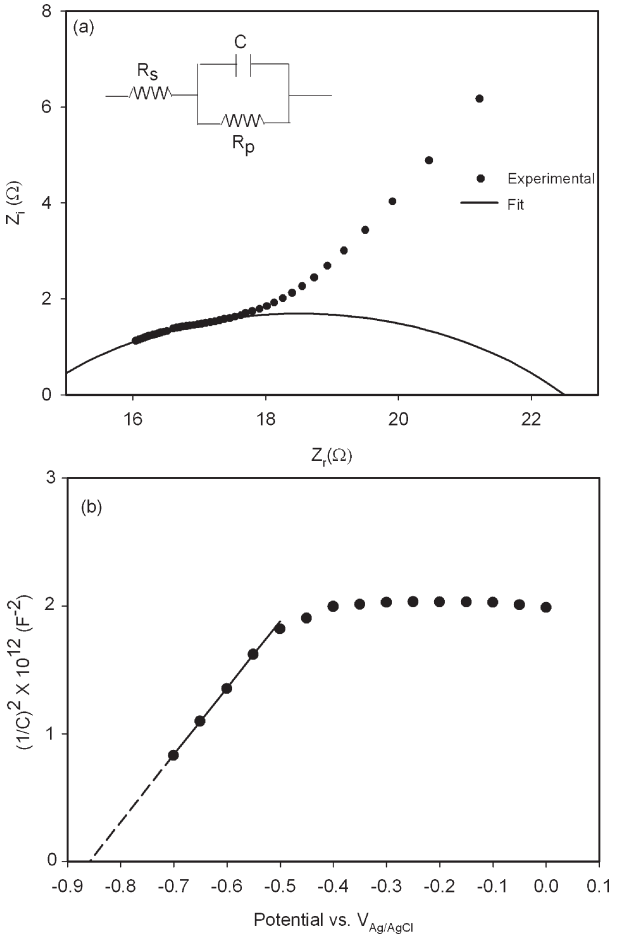

Figure 14. (a) Electrochemical impedance plot showing experimental and fitted impedance data for the α-Fe_2O_3 thin film deposited from precursor (**1**) at −0.5 V vs $V_{Ag/AgCl}$ and (b) corresponding Mott−Schottky plot. The inset of (a) shows the equivalent circuit.

influence the measured capacitance, and as a result, it is always difficult to fit the data to a simple series-parallel RC equivalent circuit which covers whole frequency range. In the present work, the data from the high frequency region where the influence of the Helmholtz layer and surface states is minimal were used to determine the space charge layer capacitance. We assumed that the electrochemical cell consisted of a simple equivalent circuit in which a resistor (R_s) was in series with a parallel pair made up of a resistor (R_p) and a capacitor. R_s is representative of the electrolyte and the electrode resistance while R_p is the resistance of the space charge layer. The parallel constant-phase element, Q, which consists of the space charge layer capacitance can be written as $Z_Q = K(j\omega)^{-n}$, where K is a constant and ω is the angular frequency. When $n = 1$, Q behaves as an ideal capacitor, whereas when $n = 0$, Q is an ideal resistor. As shown in Figure 14a, the series-parallel RC equivalent circuit fits well with the experimental values obtained in the frequency range of 25−75 kHz.

On the basis of our results shown in Figure 14b the donor density of the hematite electrode was estimated to be 2.914×10^{23} m^{-3}, and the flatband potential is approximately −0.86 V vs $V_{Ag/AgCl}$. As a result of the porosity of the electrode the effective surface area could be higher, and therefore, the true donor density could be smaller than the estimated value. However, the relatively small donor density that was estimated in this work suggests that the present method produces high quality α-Fe_2O_3 electrodes with relatively few defects.[61] As a result of the porosity of the α-Fe_2O_3 electrode and its frequency dispersion nature, the estimated flatband potential may not be accurate.[59] However, flatband potential values similar to our estimation were also reported in previous studies.[12] The film thickness estimated by taking into account the complete depletion condition of the α-Fe_2O_3 electrode yields a value of 105 nm.[62] This value is slightly higher than the value estimated from the SEM cross-sectional image (∼80 nm). The discrepancy could be a result of the frequency dispersion of the Mott−Schottky plot of porous α-Fe_2O_3 of this nature.

Conclusions

The present investigation is focused on the preparation of a single source polynuclear complex with high solubility and stability that can be used to prepare nanostructured α-Fe_2O_3 thin films by AACVD. The complex $[Fe_6(C_6H_5COO)_{10}(acac)_2(O)_2(OH)_2]\cdot 3C_7H_8$ (**1**) was synthesized by a routine chemical reaction. Structural and spectroscopic studies confirmed the identity of the hexanuclear iron(III) complex, which is highly soluble in organic solvents, stable under standard conditions, and reasonably volatile. Nanostructured α-Fe_2O_3 thin film photoelectrodes were fabricated by AACVD using the new precursor (**1**) at 475 °C in a single step without pre- or postannealing/treatments. The XRD, Raman, and XPS analyses proved that the crystalline phase is α-Fe_2O_3 and free from other forms of iron oxide. Analysis of the light absorption data shows that the optical bandgap is about 2.13 eV. The α-Fe_2O_3 film consists of 100−160 nm needle-like crystallites, which themselves are formed by incorporation of individual particles of 35 nm diameter. The electron−hole recombination is high at relatively low applied voltages (below 1.1 V vs RHE) whereas better photocurrent pulses were observed at higher voltages. The donor density of the α-Fe_2O_3 electrode was 2.914×10^{23} m^{-3}, and the flatband potential is approximately −0.86 V vs $V_{Ag/AgCl}$. The current−voltage plots recorded under AM 1.5 illumination indicated that the photocurrent onset is about 0.78 V and the photocurrent density is 600 μA cm^{-2} at 1.23 V vs RHE. This value is among the highest reported for an undoped α-Fe_2O_3 photoelectrode to date.

Our future work is directed to enhance the capabilities of the AACVD method so that using the precursor (**1**) (and other suitable precursors) the dimension of crystallites can be tuned to obtain nanostructures comparable to

(61) Liang, Y.; Enache, C. S.; van de Krol, R. *Int. J. Photoenergy* **2008**, Article ID No. 739864.
(62) van de Krol, R.; Goossens, A.; Schoonman, J. *J. Electrochem. Soc.* **1997**, *144*, 1723–1727.

the hole diffusion length of hematite which will allow us to increase the film thickness to harness all visible light up to the optical absorption threshold of α-Fe_2O_3. The present work also opens a new route to exploit novel precursor materials for AACVD to make α-Fe_2O_3 electrodes with better photoelectrochemical performance. We suggest that the highly crystalline α-Fe_2O_3 electrodes made in this work can also be used as seed layers to deposit doped α-Fe_2O_3.

Acknowledgment. We acknowledge PMI2 connect program of the British Council for partly funding the present work. We are also grateful to Dr. Sandie Dann at the Department of Chemistry, Loughborough University, for helping in XRD measurements. Pilkington Ltd. is acknowledged for kindly providing the FTO substrates for this work.

Supporting Information Available: Crystallographic information (CIF) and Table 2 (PDF). This material is available free of charge via the Internet at http://pubs.acs.org.